

RING-DIAGRAM ANALYSIS WITH GONG++

T. Corbard¹, C. Toner¹, F. Hill¹, K. D. Hanna¹, D. A. Haber², B. W. Hindman², and R. S. Bogart³

¹National Solar Observatory, 950 N. cherry Ave., Tucson, AZ 85719, USA

²JILA, Univ. of Colorado, Boulder CO 80309-0440, USA

³Stanford University, CSSA-HEPL, Stanford, CA 94305-4085, USA

ABSTRACT

Images from the updated GONG network (GONG+) have been produced since July 2001. In order to treat individual site images and the merged images (Toner et al., 2003) for local helioseismology studies, we have developed an enhanced tracking/remapping code that is now part of the new GONG pipeline (GONG++) (Hill et al., 2003). We present here the data-cube, 3D power spectra and sub-surface flow maps that will become part of the new GONG++ products and compare the preliminary results with the ring diagram analysis of MDI images for the same days.

Key words: Sun; Ring-Diagram; Data Analysis.

1. INTRODUCTION

Ring-diagram analysis of MDI images carried out over the last few years has led to a break-through in helioseismic studies which now allow us to observe the solar sub-surface flows in both azimuthal and meridional directions and in both solar hemispheres. Using this analysis technique one can study plasma dynamics around and below surface magnetic features and their evolution during the solar cycle or at smaller time scales. It remains unclear however what the uncertainties and potential bias on these measurements might be. The new high resolution GONG+ observations will allow us to test these important results with independent datasets. We present in section 2 and 3 the principal features of the code developed to perform ring-diagram analysis of GONG+ images and give in section 4 the first qualitative comparison with MDI data analysis.

2. THE ‘DATA CUBE’

In order to estimate the mean 3D velocities of an area over the Sun we need to follow this area over

time. Such a spatio-temporal area is defined by an array (or *data-cube*) of $N_x \times N_y \times N_t$ points $M_{ij}(t_k)$ identified by their heliographic latitudes $\psi_{ij}(t_k)$ and Carrington longitude $\varphi_{ij}(t_k)$ at different times t_k . In order to define such an area completely we need:

1. A reference time t_0 and a central position $M_0 = M_{00}(t_0)$ given by $\psi_0 = \psi_{00}(t_0)$ and $\varphi_0 = \varphi_{00}(t_0)$
2. A sampling time Δt so that $t_k = t_0 + k\Delta t$ for $k = -N_t/2 + 1..N_t/2$
3. The definition of a collection of points around the central position (remapping) and a tracking rate for following these points in time.

$$\left\{ \begin{array}{l} \psi_0 \\ \varphi_0 \end{array} \right. \xrightarrow{\text{remapping}} \left\{ \begin{array}{l} \psi_{ij}(t_0) \\ \varphi_{ij}(t_0) \end{array} \right. \xrightarrow{\text{tracking}} \left\{ \begin{array}{l} \psi_{ij}(t_k) \\ \varphi_{ij}(t_k) \end{array} \right.$$

4. An interpolator in order to find the values of the Doppler velocities at each point from the image pixels.

2.1. Remapping: The transverse cylindrical equidistant projection

For our local analysis, the high degree acoustic waves are assumed to be plane waves traveling across the surface of the Sun following geodesics i.e. great circles. Moreover we are going to use a 3D Fourier transform for which equidistance is assumed. Therefore we would like to have a grid on which each horizontal or vertical line is a great circle and where the distances are preserved in both directions (the equidistance in time being provided by the constant image rate Δt). In a gnomonic projection each straight line would represent a great circle but the distance scale is greatly distorted. Unfortunately, no projection can be made that preserves distance along the entire extent of the line joining any two points. However the equidistance can be insured, at least in one direction, without too much distortion near the center of the projection.

Such a projection can be obtained by placing a point of the solar surface at the coordinates $X = \psi_c$, $Y = \pi/2 - \varphi_c$ of the remapped area where ψ_c and φ_c are respectively the latitude and longitude of that point in a system where the solar meridian passing through M_0 is the new equator. Since a line of constant longitude is a great circle, all horizontal lines of the remapped area are great circles and the distances are preserved along these lines. By noting Δx and Δy the angular spacings on the remapped area and reversing the projection, we obtain:

$$\begin{cases} \psi_{ij}(t_0) = \sin^{-1}(\cos X_i \sin(Y_j + \psi_0)) \\ \varphi_{ij}(t_0) = \sin^{-1}\left(\frac{\sin X_i}{\cos \psi_{ij}(t_0)}\right) + \varphi_0 \end{cases} \quad (1)$$

where:

$$\begin{cases} X_i \equiv (i - (N_x + 1)/2) \Delta x & i = 1..N_x \\ Y_j \equiv (j - (N_y + 1)/2) \Delta y & j = 1..N_y \end{cases} \quad (2)$$

We note that the azimuthal equidistant (or Postel) projection has also been used for ring analysis (e.g. Bogart et al., 1995). This projection is constructed by projecting on a plane tangent at M_0 whereas the projection defined above and used in Haber et al. (1995) is a transverse cylindrical equidistant projection that can be obtained by projecting on a cylinder. The Postel projection is equidistant on all lines passing through M_0 but not in X nor in Y (except for $X_i = 0$ and $Y_j = 0$). More discussion about the two projections is given in the Appendix.

2.2. Tracking

The main goal of tracking is to remove as much as possible the effect of the solar rotation which would otherwise hide the small horizontal and vertical flows of interest. We consider therefore that the latitude of a point is fixed in time but its Carrington longitude is changing at a rate that is not necessarily the Carrington rate and may depend on the latitude. We use:

$$\begin{cases} \psi_{ij}(t_k) = \psi_{ij}(t_0) \\ \varphi_{ij}(t_k) = \varphi_{ij}(t_0) + (t_k - t_0) \times \\ \quad [\Omega_0 - \Omega_2 \sin^2 \psi_0 - \Omega_4 \sin^4 \psi_0 - \Omega_c] \end{cases} \quad (3)$$

where Ω_0, Ω_1 and Ω_2 are adjusted to match the sidereal differential rotation of the surface and $\Omega_c \equiv 14.1844$ deg/day is the sidereal Carrington rate. We note that the tracking is done for all points at the rate corresponding to the heliographic latitude of the center of the area. All points lying on a great circle are therefore still on a great circle after tracking. For large areas the differential rotation may vary substantially across the area and therefore one may consider tracking each point using its heliographic latitude (i.e. $\psi_{ij}(t_0)$ instead of ψ_0 in Eq. (3)). However, in the resulting sheared coordinate system, the $Y_j = \text{constant}$ lines would no longer describe great circles and it is probably better to still track the full area at a mean rate.

2.3. Interpolation

Once we know the heliographic coordinates of the points of interest we need to look for them on our solar images $I(t_k)$. The solar disc is shown on GONG+ merged images as a circle of radius r_o pixels. They are registered so that the Solar north is on top of the y axis and the east on the left. The coordinates (η, ξ) from the lower left corner of the image taken at t_k of the points $M_{ij}(t_k)$ are then obtained by doing a projection at Earth distance. If we note $\psi \equiv \psi_{ij}(t_k)$ and $\varphi \equiv \varphi_{ij}(t_k)$, we obtain:

$$M_{ij}(t_k) = I_{\eta\xi}(t_k) \quad (4)$$

where:

$$\begin{cases} \frac{\eta - \eta_c}{r_o} = \cos \psi \sin(\varphi - L_0) / (1 - S\alpha) \\ \frac{\xi - \xi_c}{r_o} = \frac{\sin \psi \cos B_0 - \cos \psi \sin B_0 \cos(\varphi - L_0)}{1 - S\alpha} \end{cases} \quad (5)$$

$$\alpha = \sin \psi \sin B_0 + \cos \psi \cos B_0 \cos(\varphi - L_0)$$

The position of the disc center (η_c, ξ_c) , its heliographic coordinates (L_0, B_0) , the Sun apparent semi-diameter in radian S and r_o can be found in the FITS header of each image¹.

The values of (η, ξ) computed from Eq. (5) are in general not integers and therefore we need to interpolate between the images' pixels. We have implemented 3 different interpolators. The 'ideal' sinc interpolator is defined in 1D by:

$$I_x = \sum_{n=-N_s}^{N_s-1} \frac{\sin(\pi(x-n))}{2N_s \tan\left(\frac{\pi(x-n)}{2N_s}\right)} I_n \quad (6)$$

where N_s defines the length of the interpolator. The 2D interpolation is obtained by applying Eq. (6) successively in each direction. This can be seen as a tapered version of the sinc interpolator where the taper is 'ideal' for the Discrete Fourier Transform (DFT) in the sense that if we were to shift the image by an arbitrary fraction of a pixel using this interpolator, with N_s equal to the number of pixels in both directions, the DFT would remain the same except for a phase difference. A similar interpolator (with a slightly different tapering function) is used during the merging of individual site images and it is probably a good idea to keep the same interpolator in both steps. However, in our current implementation, the computations needed for this interpolation are time consuming. This difficulty can be overcome by using a lookup table for the trigonometric quantities resulting in the so-called lookup sinc interpolator which has also been implemented. Finally, we have also implemented a spline interpolator based on a tensorial product of B-splines (De Boor, 1978) of arbitrary order m_s . It presents a good frequency response even for low order splines and its computation is based on finite differences which are very easy and fast to implement.

¹Respectively by the keywords: FNDLMBXC, FNDLMBYC, L0, B0, SEMIDIAM and C_LMA

By plotting the difference of the power spectra obtained from spline and sinc interpolator we realized that differences exist which are principally concentrated on the rings. These differences are however very small and the relative difference is essentially zero for absolute values of the horizontal wave number below 1 rad/Mm^{-1} . Therefore it seems that only the very outer rings could potentially be affected by the choice of the interpolation.

2.4. The ‘dense pack’ of data cubes

In order to study an extended area of the solar surface we process a collection of 189 data cubes centered at different heliographic latitudes and longitudes (ψ_0, φ_0) on the reference image $I(t_0)$.

$$\begin{cases} \psi_0(u, v) = u \times 7.5^\circ, & u = -7..7 \\ \varphi_0(u, v) = L_0(t_0) + v \times 7.5^\circ, & v = -h_{|u|}..h_{|u|} \end{cases} \quad (7)$$

where $h = [7, 7, 7, 7, 6, 6, 4, 3]$.

For the present work, we have done three dense-pack analyses for t_0 corresponding to January 2002 11-13 with corresponding $L_0(t_0) = 300^\circ, 285^\circ, 270^\circ$ respectively. We used the same parameters as in previous analyses of MDI data (e.g. Haber et al., 2002): the grid is defined by $N_x = N_y = 128$, $\Delta x = \Delta y = 0.125^\circ$, $N_t = 1664$, $\Delta t = 1 \text{mn}$; the tracking rate is given by $\Omega_0 = 451.43 \text{nHz}$, $\Omega_2 = 54.77 \text{nHz}$, $\Omega_4 = 80.17 \text{nHz}$ and the interpolator chosen is based on cubic splines ($m_s = 4$).

3. MULTITAPER ANALYSIS, RING FITTING AND INVERSION

Each data cube is then Fourier transformed via a 3D FFT. This requires first a spatial and a temporal apodization in order to avoid truncation effects. We have chosen a 2D cosine bell apodization in the spatial direction reducing a $16^\circ \times 16^\circ$ area to a circular patch of radius 15° .

The temporal apodization is carried out using a multitaper technique which first multiplies a sequence of orthogonal sine tapers to the window function, reorthogonalizes them, applies a temporal FFT to each tapered time series and then averages the resultant power spectra. Doing so, we avoid the loss of data that would result from the use of a single taper and obtain a better distribution of the power along the rings. Applying too many tapers would result in an over-smoothed power spectrum and therefore a trade-off has to be found. In this work, we used 3 sine multitapers (Fodor & Stark, 1998).

The last steps of the analysis consist in fitting the rings in the power spectra (see Fig. 1) and inverting the inferred frequency shifts to obtain the depth dependence of the flow. This has been done using the code developed for MDI and described in Bogart et al. (1995).

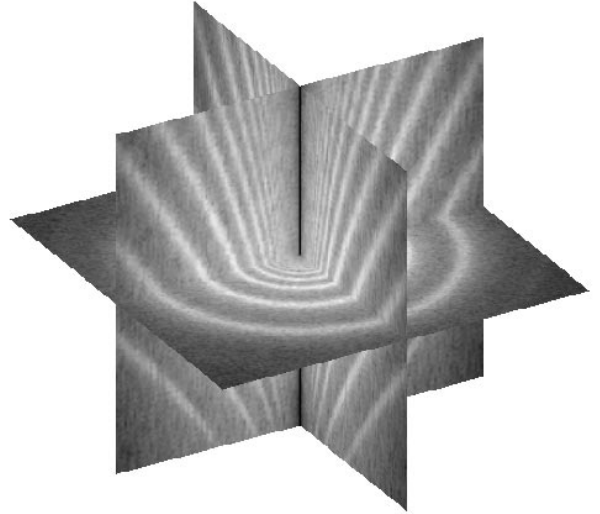


Figure 1. An example of 3D power spectra showing the characteristic rings of power distorted by the underlying flows. The two horizontal axis are k_x k_y while the vertical axis give the frequencies.

4. FIRST RESULTS: COMPARISON WITH MDI

A study of the errors as a function of depth have shown that the lowest errors are reached at a depth of about 1-2Mm. We have therefore chosen this depth for the first comparison between GONG and MDI ring diagram analysis. The differences between the flows obtained from the two datasets at a depth of 1.18 Mm are shown in Fig. 2. The amplitudes of the differences are clearly a function of the distance from the center of the disk. They remain small at the very center but can reach very high relative amplitudes at the edges. For the second day, a clear systematic difference in the orientation of the flow is found. This reflects the fact that the GONG flow for that day has been found with a significant curl. A problem with the P-angle could produce such apparent rotating flow but we couldn't identify clearly the source of the problem and why this happened only for that particular day which had a very good duty cycle of 91.2%. Clearly this is very preliminary work using the new GONG+ data product and more investigations and quantitative analysis are needed to better understand the systematic errors that may be present in both GONG and MDI data analysis.

ACKNOWLEDGMENTS

This work utilizes data obtained by the Global Oscillation Network Group (GONG) project, managed by the National Solar Observatory, which is operated by AURA, Inc. under a cooperative agreement with the National Science Foundation.

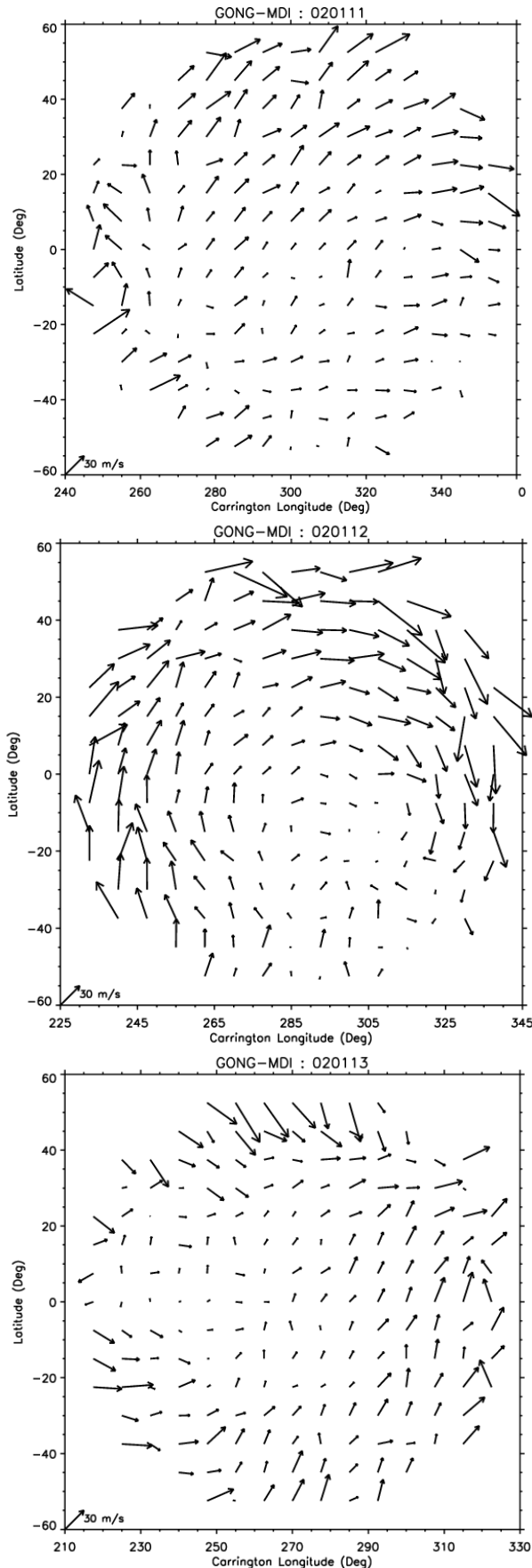


Figure 2. Difference between the flows at a depth of 1.18Mm inferred from GONG and MDI data for 3 consecutive days (January 11-13 2002 from top to bottom).

APPENDIX: AZIMUTHAL VERSUS TRANSVERSE CYLINDRICAL

As stated above, the projection used is a *transverse cylindrical equidistant projection* (or transverse plate carrée). *Cylindrical* means that it is constructed by wrapping a cylinder around the sphere. All great circles orthogonal to the one tangent to the cylinder will be remapped as parallel straight lines. It is called *transverse* because the tangent great circle chosen is not the equator but rather the solar meridian passing through M_0 . *Equidistant* means that distance is preserved along the great circles shown as horizontal lines on the remapped area. Finally we note that the points are not geometrically *projected*, in the true sense of the word, i.e. it is not a perspective projection.

The azimuthal equidistant or Postel projection is obtained by projecting on a plane tangent to the sphere at M_0 while preserving the distance along the great circles passing through M_0 . It is also not a perspective projection. It is defined by: $X_p = \theta_p \cos \varphi_p$ and $Y_p = \theta_p \sin \varphi_p$, where θ_p and φ_p are the colatitude and longitude in a system in which M_0 is at the new pole. In this system our cylindrical projection is defined by: $X = \sin^{-1}(\sin \theta_p \cos \varphi_p)$ and $Y = \tan^{-1}(\tan \theta_p \sin \varphi_p)$.

One can easily verify that $Y=\text{constant}$ is the equation of a great circle. This also shows that for small θ_p (i.e. small areas), the vertical lines also become close to great circles and our projection becomes similar to a Postel projection. For larger areas, however, the cylindrical projection does a better job in having the lines parallel to one axis describe great circles, which may be a desired feature for local plane-wave analysis, at least along one direction of propagation.

REFERENCES

- Bogart R. S., Sá L. A. D., Duvall T. L., Haber, D. A., Toomre J., and Hill F., 1995, in J. T. Hoeksema, V. Domingo, B. Fleck, and B. Battrick (eds), Proc. Fourth SOHO Workshop: Helioseismology, ESA SP-376, Vol. 2, p. 147
- De Boor C., 1978, A Practical Guide to Splines, Springer Verlag.
- Fodor & Stark, 1998, in S. Korzennik and A. Wilson (eds), Structure and Dynamics of the Interior of the Sun and Sun-like Stars, ESA SP-418, p. 171
- Haber D., Toomre, J., Hill F., Gough D., 1995, in R. K. Ulrich, E. J. Rhodes, Jr, and W. Däppen (eds), GONG'94: Helio- and Astero-seismology from the Earth and Space, ASP Conf Series 76, p. 272
- Haber A. D., Hindman B. W., Toomre J., Bogart R. S., Larsen R. M., Hill F., 2002, ApJ 570, 855
- Hill F., Bolding J., Toner C., et al., 2003, this proceeding.
- Toner C., Haber D., Corbard T., Bogart R., 2003, this proceeding.